MIT Libraries | DSpace@MIT

MIT Open Access Articles

Localized Manipulation of Magnetic Particles in an Ensemble

The MIT Faculty has made this article openly available. ***Please share*** how this access benefits you. Your story matters.

Citation: See, Hian Hian, et al. "Localized Manipulation of Magnetic Particles in an Ensemble." IEEE Access, vol. 6, 2018, pp. 24075–88. © 2013 IEEE.

As Published: http://dx.doi.org/10.1109/ACCESS.2018.2829715

Publisher: Institute of Electrical and Electronics Engineers (IEEE)

Persistent URL: http://hdl.handle.net/1721.1/118789

Version: Final published version: final published article, as it appeared in a journal, conference proceedings, or other formally published context

Terms of use: Creative Commons Attribution 3.0 Unported license

Massachusetts Institute of Technology

IEEE Access
Multidisciplinary | Rapid Review | Open Access Journal

Received February 13, 2018, accepted April 12, 2018, date of publication April 24, 2018, date of current version May 16, 2018.

Digital Object Identifier 10.1109/ACCESS.2018.2829715

Localized Manipulation of Magnetic Particles in an Ensemble

HIAN HIAN SEE[1], SAHAN C. B. HERATH[1,2], YUE DU[1], HARRY ASADA[2,3], (Member, IEEE), AND PETER C. Y. CHEN[1,2]

[1]Department of Mechanical Engineering, National University of Singapore, Singapore 117575
[2]Biosystem and Micromechanics Interdisciplinary Research Group, Singapore-MIT Alliance for Research and Technology Program, Singapore 138602
[3]Department of Mechanical Engineering, Massachusetts Institute of Technology, Cambridge, MA 02139, USA

Corresponding author: Peter C. Y. Chen (mpechenp@nus.edu.sg)

This work was supported by the A*Star Science and Engineering Research Council, Singapore through the Public Sector Funding Grant under Project 1321202077. The work of S. C. B. Herath was supported in part by the National University of Singapore and in part by the Singapore-MIT Alliance for Research and Technology Program. The work of Y. Du was supported by the China Scholarship Council.

ABSTRACT The ability to manipulate magnetic particles selectively and simultaneously (within a group of such particles) has significant implications in studying cellular behaviors and in manipulating micro-structures at an ensemble-level. The current magnetic manipulation techniques have been demonstrated to be effective for studying cell mechanics. However, they suffer from low throughput, as only one particle is addressed in an individual experiment. This renders them unsuitable for ensemble-level operations. In this paper, we present a magnetic manipulation system that enables (effectively) simultaneous yet localized manipulation of magnetic particles. The proposed system is equipped with a novel device, which realizes magnetic force localization. The properly localized force allows selective manipulation of a single magnetic particle in a group. The localization effects of this device are demonstrated and quantified through analytical modeling and simulations that yielded statistically meaningful results. With the characterized device, experiments were carried out to evaluate the effectiveness of the proposed system.

INDEX TERMS Localized magnetic force, localized manipulation, magnetic actuation.

I. INTRODUCTION

Manipulation of magnetic particles has been demonstrated to be an effective technique for investigating the mechanical behaviour of biological systems. It is applied in a wide range of studies, including the measurement of the elasticity of biopolymers, and the targeted delivery of genetic material to cells for treatment [1]–[3]. This magnetic technique is based on non-invasive manipulation of magnetic particles, where particles are typically attached to or embedded in an entity, and forces are induced by imposing a magnetic field gradient. For instance, in single cell analysis, a magnetic field is directed at a single or group of magnetic particles attached to a tethered cell to study its mechanical response to the applied forces [4], [5]. Compared to other methods (such as optical tweezers [6] and atomic force microscopy [7]), magnetic manipulation offers the advantage in terms of (i) low power requirements, (ii) reconfigurable forces and torques, (iii) absence of sample photodamage, and (iv) high force gradients over relatively larger distance.

The ability to precisely manipulate a single magnetic particle (within a group of such particles) has potential applications in studying cellular and molecular behaviors at an ensemble-level (where significant events of cell-cell and cell-environment interactions occur) and in enabling more sophisticated ways of manipulating cells, biomolecules, micro-robots, and other micro-structures. One possible application is in the mechanical manipulation of extracellular matrix (ECM) stiffness for the investigation of cell-matrix mechanical interactions [8]–[11]. This involves embedding magnetic particles in the ECM through bioconjugation (with the particles firmly attached to the collagen fibers in the ECM), and then employing a localized magnetic force to anchor the particles (individually) in their nominal positions while they are subjected to possible cellular forces. This form of anchoring of the particles impedes the movements of the collagen fibres, thus possibly results in a change of apparent stiffness of the ECM as sensed by the cells. Such an ECM stiffness manipulation could provide insight as to how cells process cues from their surrounding environment

 This work is licensed under a Creative Commons Attribution 3.0 License. For more information, see http://creativecommons.org/licenses/by/3.0/

and could also offer new opportunities to tailor a cell's local microenvironment in a biologically relevant fashion.

The key to selectively manipulating a single magnetic particle in an ensemble lies in the localization of the magnetic force. The extent of this localization gives rise to the issue of proximity interference, where the magnetic field gradient intended for a specific particle may exert a force on another particle nearby, hence causing it to dislocate from its prescribed location. A properly localized magnetic force may offer a viable solution for addressing this issue.

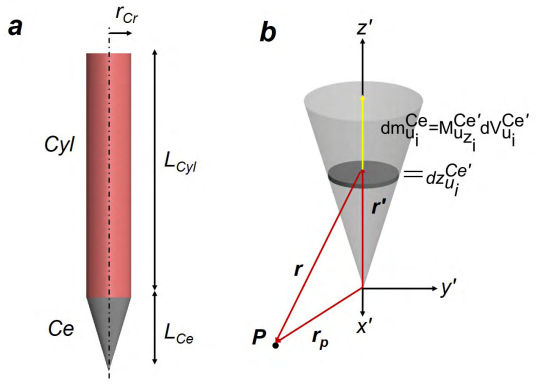

FIGURE 1. (a) Schematic illustration of the soft magnetic core. (b) Conical component of the core. The shaded areas represent the elementary magnetic dipole.

For this case, the magnetic field generator plays a crucial role in enabling the device to selectively control a targeted particle in a group. This has led to the development of a *miniaturized* electromagnetic needle (EMN) [12], [13]. The EMN consists of an electromagnetic coil wrapped around a soft magnetic core. The core is made of high magnetic permeability/saturation material to produce a large magnetic field gradient. The design of the core (as illustrated in Fig. 1(a)) is represented by an axially symmetrical cylindrical shank (i.e. *Cyl*, shaded in red) with a protruding conical tip (i.e. *Ce*, shaded in grey). The tip geometry is designed to concentrate the emanated magnetic flux. However, several technical challenges remain in the application of the *miniaturized* EMN. First, the size of the micro-scale EMN inherently limits the magnitude of the generated field gradient and consequently, the magnetic force induced on the particle is weak. Second, the fabrication of the micro-scale EMN may be challenging due to its size and complex three-dimensional (3D) geometry. The fabrication of the 3D micro-scale electromagnetic coil involves complicated procedures such as repeated lithography, thick photoresist processing, and electroplating [14]–[16]. As for the protruding magnetic core, harsh chemicals and etching conditions are required to remove the substrate underneath, which may cause material incompatibility.

In this paper, the objective is to develop an engineering solution that enables (effectively) simultaneous yet localized manipulation of magnetic particles in an ensemble. The scope of this work is twofold.

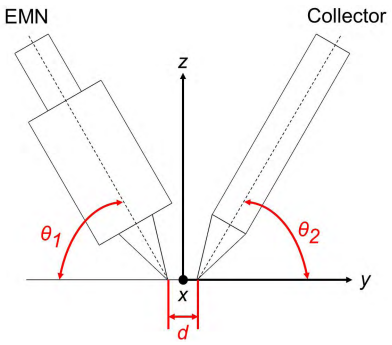

FIGURE 2. Schematic diagram of the EMNC. Parameter d is the distance between the tips of the EMN and the flux collector. Parameter θ_u is the angle of inclination (with respect to the horizontal axis), and the subscripts $u = 1$ and $u = 2$ refer to the EMN and collector, respectively.

First, we proposed a novel magnetic device (as illustrated in Fig. 2) that uses an EMN and a flux collector strategically positioned relative to each other to realize magnetic field (and force) localization. This flux collector is identical to the soft magnetic core of the EMN and it operates as a magnetic field sink. The collector provides a path for the magnetic field emanating from the EMN tip, therefore reducing its distribution and concentrating the field in the region between the EMN and collector tips. We refer to this device as the EMN-collector assembly (i.e. EMNC). Next, the analytical modelling of the induced magnetic field (and force) by the EMNC assembly is established. We then performed simulations with the devised models to evaluate the localization effects of the EMNC assembly (in terms of magnetic field and force) under different configurations.

Second, we developed a magnetic manipulation system equipped with the characterized EMNC assembly to realize the proposed approach of (effectively) simultaneous yet selective manipulation of magnetic particles in a group. A set of experiments were conducted with the developed system to demonstrate its effectiveness.

The remainder of this paper is organized as follows. Section II describes and validates the analytical models of the EMNC assembly for determining the magnetic field and force. Section III evaluates the localization effects of the magnetic field and force under different EMNC configurations. Section IV presents the magnetic manipulation system for selectively manipulating multiple magnetic particles and its experimental results. Section V concludes the paper and recommends possible further improvements.

II. MAGNETIC INDUCTION MODELLING

A. MAGNETIC FIELD MODELLING

We based the analytical model for calculating the magnetic field $\mathbf{B_{ec}}$ produced by an EMNC assembly on a system of magnetic dipoles [17], [18]. One superimposes the magnetic fields produced by (i) the EMN and (ii) the flux collector to obtain the resultant magnetic flux density $\mathbf{B_{ec}}$ at any given point in the workspace $\mathbf{P}$ (i.e., any point outside the EMNC), with the coordinates (x, y, z), which can be expressed by the

vector $\mathbf{B_{ec}}(\mathbf{P}) \in \mathbb{R}^{3\times 1}$, i.e.,

$$\mathbf{B_{ec}}(\mathbf{P}) = \sum_{u=1}^{2} \mathbf{B_u}(\mathbf{P}) \tag{1}$$

where $\mathbf{B_1}(\mathbf{P})$ and $\mathbf{B_2}(\mathbf{P})$ refer to the magnetic fields of the EMN and the flux collector, respectively (i.e. the subscripts $u = 1$ and $u = 2$ refer to the EMN and collector, respectively). It has to be noted that the magnetic field $\mathbf{B}$ can also be described by $\mathbf{H}$ in units ampere per meter with $\mathbf{B} = \mu_0\mathbf{H}$, where $\mu_0 = 4\pi \times 10^{-7}$Tm/A is the magnetic constant.

The magnetic field $\mathbf{B_u}$ at $\mathbf{P}$ can be determined by considering the magnetic core as a set of magnetic dipoles. These dipoles generate a set of individual magnetic scalar potentials which, when superimposed, yield the total magnetic scalar potential $\phi_{u_t}(x, y, z) \in \mathbb{R}$ produced by the device u. Then we have the associated magnetic field at $\mathbf{P}$, i.e.,

$$\begin{aligned}\mathbf{B_u}(\mathbf{P}) &= \mu_0\mathbf{H_u}(\mathbf{P}) \\ &= -\mu_0\nabla\phi_{u_t} \\ &= -\mu_0\left[\frac{\partial\phi_{u_t}}{\partial x}, \frac{\partial\phi_{u_t}}{\partial y}, \frac{\partial\phi_{u_t}}{\partial z}\right]^T.\end{aligned} \tag{2}$$

An elementary magnetic dipole with a volume of dV' and a magnetization $\mathbf{M} \in \mathbb{R}^{3\times 1}$ has a magnetic moment $d\mathbf{m}$, i.e.,

$$d\mathbf{m} = \mathbf{M}dV' \tag{3}$$

which creates an elementary magnetic scalar potential $d\phi$ at $\mathbf{P}$ that can be expressed as

$$d\phi = \frac{1}{4\pi}\frac{\mathbf{r}\cdot d\mathbf{m}}{r^3} = \frac{1}{4\pi}\frac{\mathbf{r}\cdot\mathbf{M}}{r^3}dV' \tag{4}$$

where $\mathbf{r} = \mathbf{r_p} - \mathbf{r}'$ is the relative position vector, which points from the elementary dipole to the point $\mathbf{P}$ and $r = \|\mathbf{r}\|_2$ (i.e. l_2- norm of $\mathbf{r}$) is the distance between the elementary dipole and $\mathbf{P}$.

The magnetic core of the device u is represented by two parts, namely, (i) Ce_u, and (ii) Cyl_u. The geometry of the magnetic core dictates that the dominant component of the core magnetization to align and vary along its longitudinal axis (i.e. z'_u-axis). Therefore, $\mathbf{M_u}$ can be expressed as,

$$\mathbf{M_u} = \left[M_{u_x}, M_{u_y}, M_{u_z}\right]^T \approx \left[0, 0, M_{u_z}(z'_u)\right]^T \tag{5}$$

The total magnetic scalar potential of device u, ϕ_{u_t} is determined by partitioning Ce_u to N numbers of dipoles along the $z_u^{Ce'}$-axis (i.e. z'_u-axis of Ce_u). This is realized by dividing the interval $[0, L_{Ce_u}]$ into sub-intervals of $\{[z_{u0}^{Ce'}, z_{u1}^{Ce'}], [z_{u1}^{Ce'}, z_{u2}^{Ce'}], \ldots, [z_{uN-1}^{Ce'}, z_{uN}^{Ce'}]\}$, with each dipole spanning a sub-interval $[z_{u_{i-1}}^{Ce'}, z_{u_i}^{Ce'}]$. Each Ce_u dipole is modelled as a circular disk of thickness $dz_{u_i}^{Ce'}$ and has a volume of $dV_{u_i}^{Ce'}$ with a magnetization $M_{u_{z_i}}^{Ce'}$, as illustrated in Fig. 1(b). As the scalar potentials decay rapidly with $1/(r_{u_i})^3$, the contributions of Cyl_u to ϕ_{u_t} are assumed to be negligible. The ϕ_{u_t} at $\mathbf{P}$ is then approximated by the summation of the scalar potential of every Ce_u dipole (i.e. $\phi_{u_i}^{Ce}$) over the length of Ce_u (for the details of $\phi_{u_i}^{Ce}$, refer to Appendix A), that is,

$$\phi_{u_t}(x, y, z) = \sum_{i=1}^{N} \phi_{u_i}^{Ce}(x, y, z) \tag{6}$$

By substituting (6) into (2), the magnetic field $\mathbf{B_u}$ at point $\mathbf{P}$ can be evaluated.

The magnetic field $\mathbf{B_u}$ is dependent on the magnetization of the Ce_u dipoles. For the case of EMN (i.e. $u = 1$), the $M_{1_{z_i}}^{Ce'}$ is dependent on the current passing through the electromagnetic coil wrapping around the Cyl_1. This implies that $M_{1_{z_i}}^{Ce'}$ is a function of the magnetic field strength $H_{sCyl_1}(z_{1_i}^{Ce'})$, which is the summation of the field contributions by the coil and the magnetized Cyl_1 (for the details of $H_{sCyl_1}(z_{1_i}^{Ce'})$, refer to Appendix B). As for the case of flux collector (i.e. $u = 2$), the $M_{2_{z_i}}^{Ce'}$ is induced by the EMN. In consequence, $M_{2_{z_i}}^{Ce'}$ is a function of the magnetic field strength $H_1(z_{2_i}^{Ce'})$, and owing to the geometry of the conical-shaped tip, the magnetic flux is concentrated. For that reason, the field strength $H_1(z_{2_i}^{Ce'})$ is amplified along the length of Ce_2, and the relationship is governed by

$$H_1(z_{2_i}^{Ce'}) \propto \frac{1}{A_{Ce}(z_{2_i}^{Ce'})/A_{Ce}(z_{2_N}^{Ce'})} \tag{7}$$

where $A_{Ce}(z_{2_i}^{Ce'})$ is the cross sectional area of Ce_2 at $z_{2_i}^{Ce'}$.

The values of $M_{u_{z_i}}^{Ce'}$ can be evaluated from the magnetization curve of the core material. The curve can be approximately defined by the Langevin function,

$$M_{u_{z_i}}^{Ce'}(H_k) = M_{sat}(coth(aH_k) - \frac{1}{aH_k}) \tag{8}$$

where

$$H_k = \begin{cases} H_{sCyl_1}(z_{1_i}^{Ce'}), & \text{if } M_{u_{z_i}}^{Ce'} = M_{1_{z_i}}^{Ce'} \\ H_1(z_{2_i}^{Ce'}), & \text{if } M_{u_{z_i}}^{Ce'} = M_{2_{z_i}}^{Ce'} \end{cases}$$

The M_{sat} term is the saturated magnetization of the material and factor a is related to the other physical properties [19].

A global coordinate system is used, the origin of which is located at the centre of the workspace (as shown in Fig. 2). The coordinates of the workspace are transformed to the local coordinate system of each individual device u (i.e. the EMN and the flux collector, respectively), with the origin located at the tip of the device. Next, the components of the magnetic field due to each device u are then calculated. Subsequently, the components of the magnetic field are transformed back to the global coordinate system, where they were superimposed to obtain the global magnetic field $\mathbf{B_{ec}}(\mathbf{P})$.

B. EXPERIMENTAL VALIDATION OF MAGNETIC FIELD

1) EXPERIMENT SETTING

To investigate the validity of the magnetic field model, we positioned an EMNC in the configuration, as illustrated in Fig. 2. This configuration serves to establish a common

TABLE 1. Configurations of the EMNC for model validation.

Magnetic field component	Input current (A)	d (mm)	$\theta_1 = \theta_2$ (°)	$[x, y, z]$ (mm)	RMSE (mT)
$B_{ec_z}(z)$	0.1	0.989	50	[0.00, 1.42, z]	0.0667
$B_{ec_y}(x)$	3	0.396	60	[x, 1.10, 1.50]	0.0186
$B_{ec_x}(y)$	2	0.439	60	[1.40, y, 0.40]	0.1417

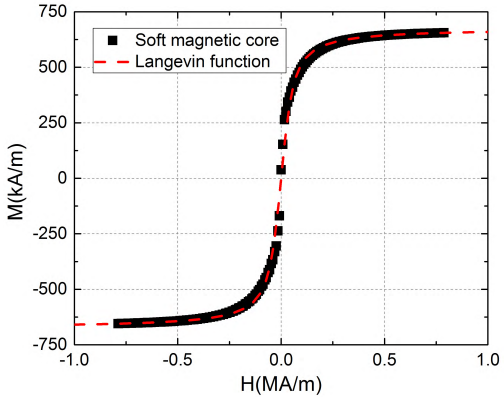

FIGURE 3. Magnetization curve of the soft magnetic core. Data points are acquired with the vibrating sample magnetometer.

basis for comparing the results from the model and the experiments. The fabricated EMN has a magnetic core of 69 mm cylindrical length (with a radius of 6.35 mm) and a conical height of 21 mm terminating with a tip radius of 33.25 μm. The core is made of a soft magnetic material (i.e. hysteretic effects are negligible) with a magnetization curve as reported in Fig. 3. This curve is experimentally obtained using a vibrating sample magnetometer (Model 7407, Lake Shore Cryotronics, Inc., Westerville, OH). The flux collector is fabricated to be identical to the core of the EMN. The EMN and the collector are then assembled with a custom-designed aluminium holder, which provides mechanical support without interfering with the emanated magnetic fields. Furthermore, this holder also acts as an excellent heat sink since aluminium has a high thermal conductivity and this allows rapid dissipation of any possible heat generated by the EMNC.

The magnetic field of the EMNC is characterized using a gauss meter equipped with a hall sensor probe (Model GM07, Hirst Magnetic Instruments Ltd, Cornwall, UK). The probe measures the magnetic field lines that are perpendicularly passing through its sensing element. The EMNC assembly is mounted on a three-axis motor-driven positioning stage, with a travel range of 100 mm in all directions and a step resolution of 2 μm. The stage is used to precisely control the relative distance between the EMNC tips and the hall sensor probe.

2) EXPERIMENT PROCEDURE

Three sets of experiments were conducted to characterize the magnetic field components of $B_{ec_x}(y)$, $B_{ec_y}(x)$, and $B_{ec_z}(z)$. The specific configurations of the EMNC for the experiments are listed in Table 1. The hall sensor probe is placed away from the EMNC tips to prevent possible collision damage. The magnetic field components were measured at a regular interval of 0.1 mm. For the magnetic field $B_{ec_z}(z)$, the EMNC is shifted along the $z-$ axis (away from the stationary probe) from 0.2 mm to 2 mm. Similarly, for the magnetic fields $B_{ec_x}(y)$ and $B_{ec_y}(x)$, the EMNC is displaced along the $y-$ and $x-$ axis from -1.5 mm to 1.5 mm, respectively.

3) EXPERIMENTAL RESULTS

The experimental data was quantitatively compared with the computed values from the magnetic field model. It is found that there were discrepancies between the measured and calculated results. However, by introducing a multiplicative scaling function of $c_u I^{v_u}$ (where I is the input current of the EMN, and c_u and v_u are the fitted parameters, the subscripts $u = 1$ and $u = 2$ refer to the EMN and flux collector, respectively) to the magnetic fields $\mathbf{B_1}$ and $\mathbf{B_2}$ separately, we are able to achieve a good agreement between the two results. When we compare the values of the magnetic fields predicted by the model to those measured experimentally, we find the R-squared and the root mean square error (RMSE) to provide indicators of how close the values are to each other. A comparison between the computed (with $c_1 = 0.55$, $v_1 = 0.6$, $c_2 = 0.29$ and $v_2 = 0.51$) and the measured results is shown in Fig. 4, and the specific RMSE values are provided in Table 1.

C. MAGNETIC FORCE MODELLING

The position and orientation of a soft-magnetic particle can be controlled by the applied magnetic force and torque. With the soft-magnetic materials (where hysteretic effects are negligible), the magnetization of the particle is dependent on the applied magnetic field. In the context of manipulating a soft-magnetic *spherical* particle, no magnetic torque will be generated on the particle [20]. The reason is that there is no shape anisotropy, and the magnetization vector will always align itself with the induced magnetic field.

For the translational manipulation, the force that a magnetic field gradient applies to a spherical micron-sized soft-magnetic particle with a magnetic moment of $\mathbf{m_p} \in \mathbb{R}^{3\times1}$ is described by

$$\mathbf{F_p} = (\mathbf{m_p} \cdot \nabla)\mathbf{B_{ec}} \tag{9}$$

Since there is no electric current flowing through the region occupied by the particle, the *Maxwell's* equations provide the

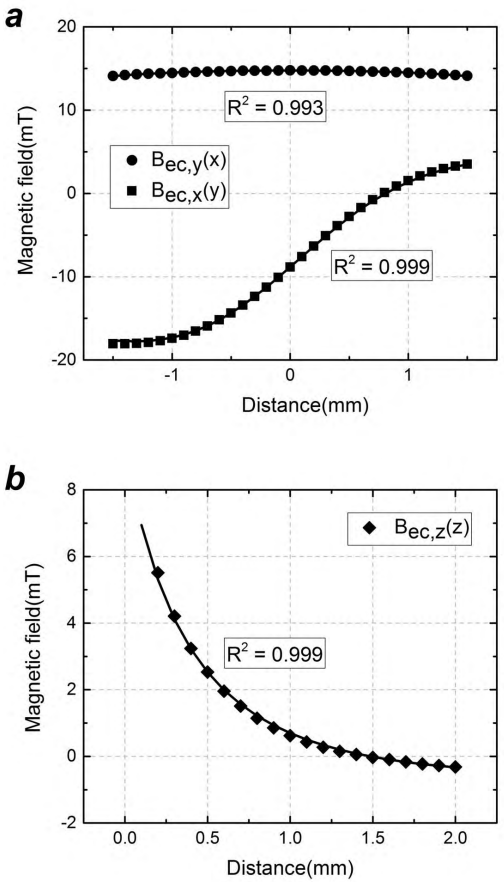

FIGURE 4. Comparison of the calculated and experimentally evaluated magnetic fields. (a) Magnetic fields $B_{ec_x}(y)$ and $B_{ec_y}(x)$. (b) Magnetic fields $B_{ec_z}(z)$. Data points are measurements with the hall probe. Solid lines are computed values from the analytical model.

constraint $\nabla \times \mathbf{B_{ec}} = 0$ [21], and this allows us to rewrite (9) as

$$\mathbf{F_p} = \begin{bmatrix} \frac{\partial B_{ec_x}}{\partial x} & \frac{\partial B_{ec_y}}{\partial x} & \frac{\partial B_{ec_z}}{\partial x} \\ \frac{\partial B_{ec_x}}{\partial y} & \frac{\partial B_{ec_y}}{\partial y} & \frac{\partial B_{ec_z}}{\partial y} \\ \frac{\partial B_{ec_x}}{\partial z} & \frac{\partial B_{ec_y}}{\partial z} & \frac{\partial B_{ec_z}}{\partial z} \end{bmatrix} \begin{bmatrix} v_p M_{p_x} \\ v_p M_{p_y} \\ v_p M_{p_z} \end{bmatrix} \tag{10}$$

where v_p is the volume of the particle and M_p is the magnetization of the particle. The values of M_p can be evaluated from the magnetization curve of the particle.

III. LOCALIZATION EFFECTS OF EMNC

To understand the localization effects of the EMNC assembly on the magnetic field and force, simulations were performed using the analytical models derived in Section II. We parameterized the distance between the tips of the EMN and the flux collector (d), and the angle of inclination (θ_u, with the subscripts $u = 1$ and $u = 2$ refer to the EMN and collector, respectively). Then, the localization effects are systematically evaluated by changing the parameters independently. The localization effects are assessed by identifying a localized area (i.e. half-power region), within which the magnitude of the induced magnetic field (or force) is greater than 70.7% of the maximum value [22]. To evaluate the proposed device, the localization effects of those without the flux collector (i.e. only the EMN) are compared with the EMNC assembly. This works by utilizing the threshold value that was used to determine the localized area of the EMN to evaluate the localization effects of the corresponding EMNC configurations (with the same parameter θ_1 and input current).

For the simulations, we have chosen an EMNC assembly with the specifications as reported in Section II-B, and due to the physical characteristics of the EMNC, there is only sufficient space to accommodate a θ_u that ranges from 40° to 60°. The localization effects were evaluated within a 10 by 10 mm^2 planar area and at a $z = -0.1$ mm plane of the workspace. In the simulations, the EMN is simulated with an input current of 0.1 A, and the parameters were varied (over the following ranges: $d = 0.1$ mm to 1.7 mm, and $\theta_u = 40°$ to 60°) in the four scenarios below to investigate the effects of the parameters on magnetic field and force localization:

(1) the distance between the EMNC tips (i.e. varying d with $\theta_1 = \theta_2$ fixed at 60°);
(2) the angles of inclination for both the EMN and flux collector (i.e. varying $\theta_1 = \theta_2$ with d fixed at 0.1 mm);
(3) the angle of inclination for the EMN (i.e. varying θ_1 with d and θ_2 fixed at 0.1 mm and 60°, respectively);
(4) the angle of inclination for the flux collector (i.e. varying θ_2 with d and θ_1 fixed at $= 0.1$ mm and 60°, respectively).

The simulations were facilitated with MATLAB and were performed iteratively.

A. MAGNETIC FIELD LOCALIZATION

Fig. 5(a) depicts the localized area of the l_2- norm of the magnetic field, which is outlined by a black color boundary. The detailed simulation results of the magnetic field localization are reported in Fig. 6. The simulations revealed that as the parameter d reduces, a clear improvement of the field localization with the collector is shown in Fig. 6(a). Specifically, for $d = 0.1$ mm, it is found that the localized area of the EMNC is drastically reduced by 78.86% compared to the EMN. With regard to the parameters $\theta_{1=2}$ (i.e. $\theta_1 = \theta_2$), the simulation results are depicted in Fig. 6(b). The results show that as $\theta_{1=2}$ increases, the localized area of the EMNC reduces, and with $\theta_{1=2} = 60°$, the localized area of the EMNC is 4.73 times smaller than the EMN. However, if $\theta_{1=2} < 41°$, the effect of the collector in localizing the magnetic field diminishes. Fig. 6(c) and Fig. 6(d) depict the respective simulation results of θ_1 and θ_2 on the magnetic field localization. Both parameters θ_1 and θ_2 exhibited a monotonic decrease in the localized field area (i.e. the localization effects of the EMNC becomes more prominent) with increased parameter value. These results suggest that the localized field area could be controlled by either configuring the EMN or the collector individually.

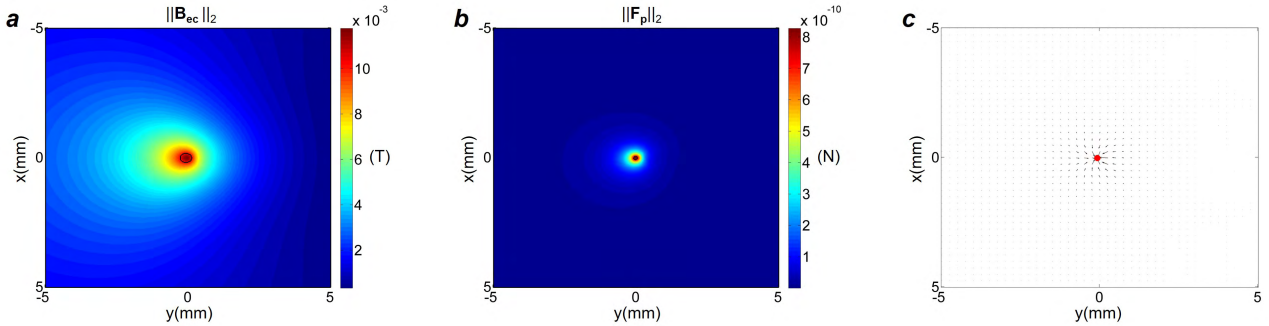

FIGURE 5. Localized area of an EMNC assembly with the parameters $d = 0.1$ mm and $\theta_{1=2} = 60°$ (outlined with a black color boundary): (a) l_2- norm of magnetic field, and (b) l_2- norm of magnetic force. (c) Two-dimensional vector field of the magnetic force (with the zero force point marked by the red color circle).

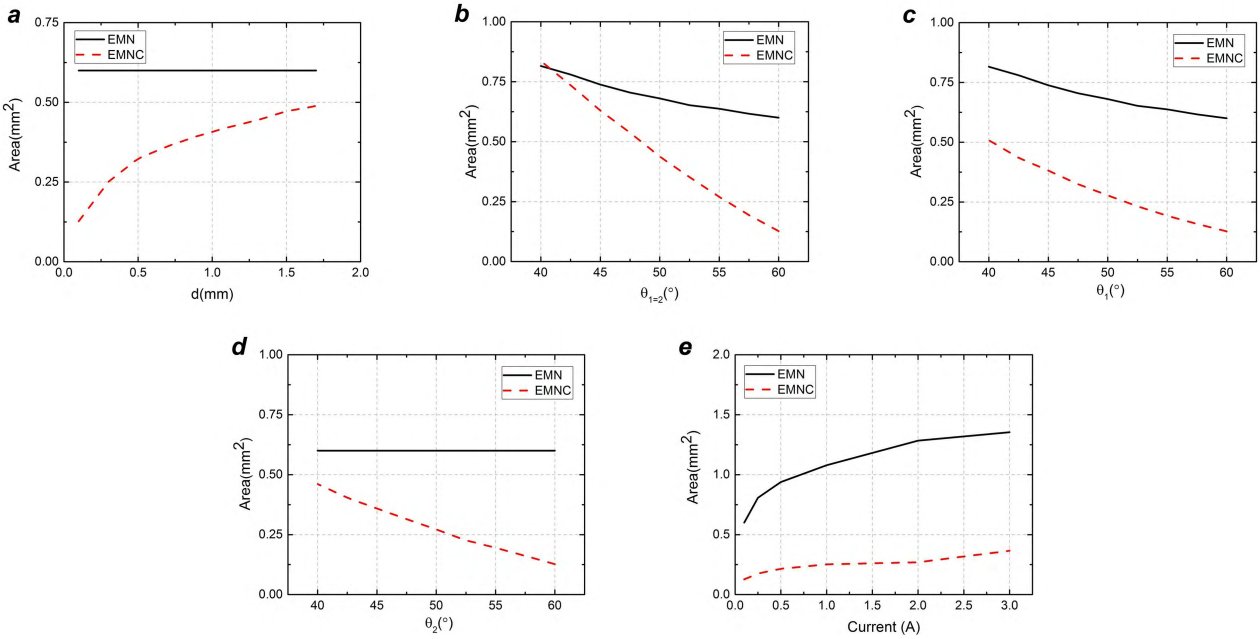

FIGURE 6. Magnetic field localization. Output of the simulations with the magnetic field model: (a) parameter d was varied from 0.1 mm to 1.7 mm with $\theta_{1=2}$ fixed at 60°, (b) parameters $\theta_{1=2}$ was varied from 40° to 60° with d fixed at 0.1 mm, (c) parameter θ_1 was varied from 40° to 60° with d and θ_2 fixed at 0.1 mm and 60°, respectively, and (d) parameter θ_2 was varied from 40° to 60° with d and θ_1 fixed at 0.1 mm and 60°, respectively. (e) The optimal configuration of EMNC with $d = 0.1$ mm and $\theta_{1=2} = 60°$, and the input current was varied from 0.1 A to 3 A.

B. MAGNETIC FORCE LOCALIZATION

For the study of the localization effects on the magnetic force, the simulated forces are applied on paramagnetic particles with a diameter of 100μm. The magnetization curve of the paramagnetic particle is reported in Fig. 7. This curve can be approximately described by the Sum of Sines model with four terms in the series,

$$M = \sum_{w=1}^{4} a_w \sin(b_w H + c_w) \tag{11}$$

where a_w, b_w and c_w are fitted parameters. The fitted curve is depicted in Fig. 7, which has a R-squared of 0.999 and a RMSE of 0.0092.

Fig. 5(b) depicts the localized area of the l_2- norm of the magnetic force, which is outlined by a black color boundary. The two-dimensional force vector field is presented in Fig. 5(c), it is revealed that the magnetic forces would direct particles in the $x-y$ plane to the zero force point (which is marked by the red color circle). A magnetic particle that is at the zero force point would reach an equilibrium in the $x - y$ plane. The detailed simulation results of the magnetic force localization are reported in Fig. 8 and it was observed to have similar trends to the results of magnetic field localization. The simulation results depicted in Fig. 8(a) indicate that as the parameter d decreases, the effectiveness of the collector in localizing the magnetic force is more apparent, and with $d = 0.1$ mm, the localized area of EMNC

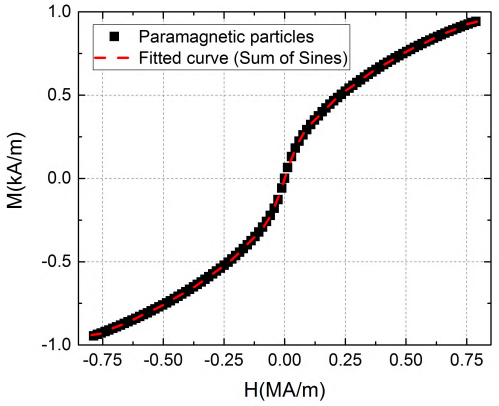

FIGURE 7. Magnetization curve of the paramagnetic particle with a diameter of 100μm. Data points are acquired with the vibrating sample magnetometer.

is minimized to a size of 2.83 times smaller than the EMN. As for the parameter $\theta_{1=2}$, the simulation results in Fig. 8(b) revealed that a larger $\theta_{1=2}$ corresponds to a smaller localized area of EMNC. Specifically, with $\theta_{1=2} = 60°$, the localized area of EMNC is greatly reduced by 64.64% compared to the EMN. However, if $\theta_{1=2} < 50.75°$, the advantage of using the collector in localizing the magnetic force disappears. The simulation results of the effects of the parameters θ_1 and θ_2 on the magnetic force localization are shown in Fig. 8(c) and Fig. 8(d), respectively. The results indicate that as θ_1 (or θ_2) increases, the localized area of the EMNC decreases. This shows the influences of these two parameters on the magnetic force localization independently. However, it is noted from Fig. 8(d) that if $\theta_2 < 47°$, the collector has no effect in localizing the magnetic force. This observation suggests that configuring the EMN would be more desirable (than configuring the collector) in localizing the magnetic force, since the localization effects are not limited by the variations of θ_1.

C. OPTIMAL CONFIGURATION OF EMNC

Based on the simulation results of the magnetic field and force localization, we determined an optimal configuration for the EMNC, that is $d = 0.1$ mm and $\theta_{1=2} = 60°$. Based on this configuration, simulations were performed to examine the localization effects of the EMNC (on the magnetic field and force) over a range of input current from 0.1 A to 3 A, and the results are reported in Fig. 6(e) and 8(e), respectively. The results indicated that the localized area of the EMNC is systemically lower than the EMN and this shows that the inclusion of the flux collector does effectively concentrate the magnetic field and force.

D. VISUALIZATION OF LOCALIZATION EFFECTS

An experiment was conducted to provide a visualization of the localization effects of the EMNC assembly. This experiment involves the tracking of the movements of the iron filings in a (purchased off-the-shelf) two-dimensional magnetic field demonstrator. In the experiment, the EMN and the EMNC were positioned above the magnetic field demonstrator, and the movements of the iron filings were filmed when the EMN (with the configuration of $\theta_1 = 60°$) and then the EMNC (with the configuration of $\theta_{1=2} = 60°$ and $d = 0.329$ mm) were supplied with an input current of 3 A. Fig. 9 was captured via an imaging unit, which was fixed below the magnetic field demonstrator, and it shows the demonstrator under the EMN and the EMNC after the input current was supplied. It can be observed from Fig. 9(a) that the area-of-influence of the single EMN (which is outlined by a red color boundary) is approximately 2.17 times larger than the EMNC assembly (as depicted in Fig. 9(b)). The area-of-influence indicates the region of the iron filings in the demonstrator, which was affected by the generated magnetic field and force. This experimental result provides direct evidence that the EMNC assembly was effective in localizing the generated magnetic field and force, which only affected the iron filings that were nearest to its tips.

IV. LOCALIZED MANIPULATION OF MAGNETIC PARTICLES

In this section, we report the development of a magnetic manipulation system equipped with an EMNC assembly for (effectively) simultaneous yet selective manipulation of multiple magnetic particles. The design of the manipulation system is first described, which is followed by the visual tracking algorithm of multiple particles, the control scheme, and the experimental results.

A. MAGNETIC MANIPULATION SYSTEM

To achieve (effectively) simultaneous manipulation of multiple magnetic particles, we first establish a magnetic manipulation system, as shown in Fig. 10. The system consists of three sub-systems for execution, sensing, and control. The executive sub-system comprises a three-axis motorized stage (with a travel range of 100 mm in all directions and a step resolution of 2 μm) and an EMNC assembly (with $d = 0.264$ mm and $\theta_{1=2} = 60°$) connected to a programmable power supply. The EMNC assembly is mounted to the stage and it functions as an end-effector to manipulate the particles. The sensory sub-system comprises of a high resolution distortion-less macro lens connected to a high speed CMOS camera (which is specified to film at a maximum 90 frames-per-second with full resolution of 2048 by 2048 pixel^2). The imaging system is inverted with the light source on the top, illuminating light down to the workspace. The control sub-system receives the visual feedback from the camera and generates the required outputs. The control software is developed in MATLAB for automatic manipulation.

B. TRACKING OF MULTIPLE MAGNETIC PARTICLES

In the automatic manipulation process, the tracking of the magnetic particles plays an important role in supplying the feedback of the particles' positions. We first implement the center of mass algorithm to estimate the positions of the particles, and this algorithm includes three major operations. First, the images are converted from the original images into grayscale images. Second, due to the highly opaque particles,

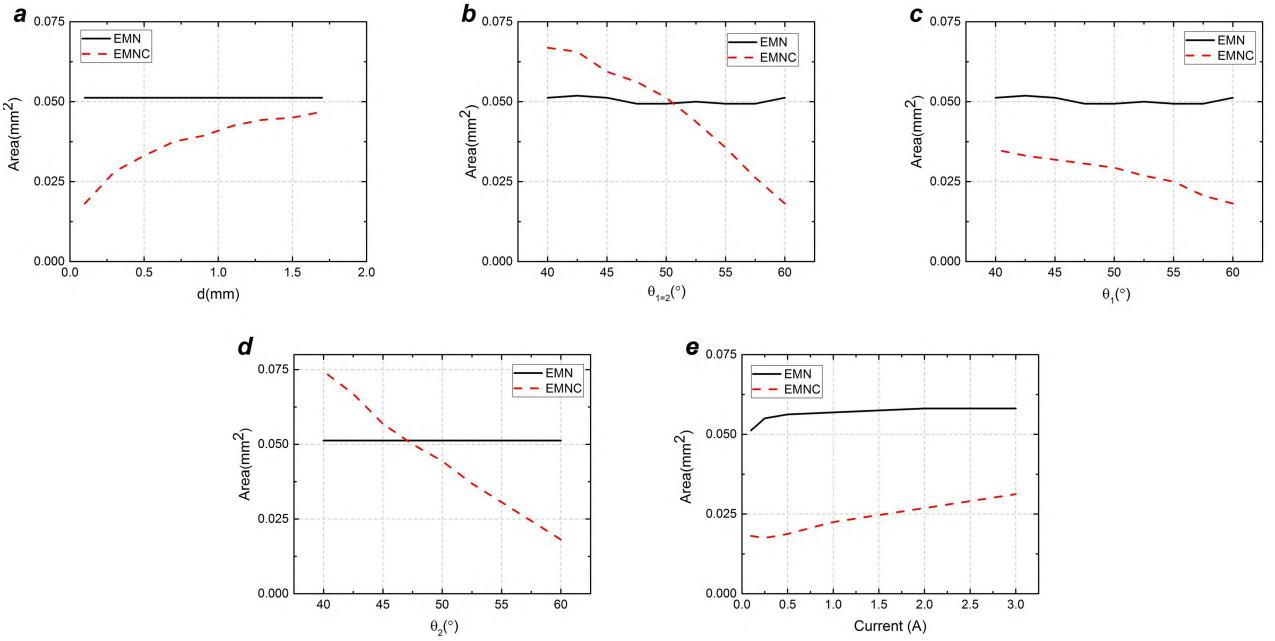

FIGURE 8. Magnetic force localization. Output of the simulations with the magnetic force model: (a) parameter d was varied from 0.1 mm to 1.7 mm with $\theta_{1=2}$ fixed at 60°, (b) parameters $\theta_{1=2}$ was varied from 40° to 60° with d fixed at 0.1 mm, (c) parameter θ_1 was varied from 40° to 60° with d and θ_2 fixed at 0.1 mm and 60°, respectively, and (d) parameter θ_2 was varied from 40° to 60° with d and θ_1 fixed at 0.1 mm and 60°, respectively. (e) The optimal configuration of EMNC with $d = 0.1$ mm and $\theta_{1=2} = 60°$, and the input current was varied from 0.1 A to 3 A.

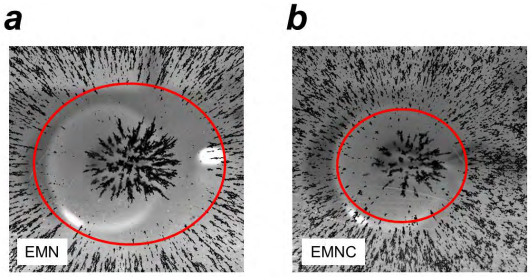

FIGURE 9. Visualization of the localization effects with a two-dimensional magnetic field demonstrator. Images (a) and (b) show the demonstrator under the EMN and the EMNC assembly after the input current was supplied. The area-of-influence of the EMN and the EMNC assembly are outlined with a red color boundary.

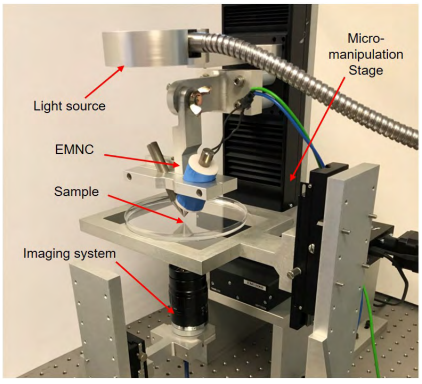

FIGURE 10. Experimental setup for magnetic control of multiple microscopic particles under the vision feedback guidance.

the images have a clear contrast between the particles and the background. Hence, the profiles of the particles are easily detected by a threshold value. Last, the central positions (i.e. two-dimensional coordinates) of the particles are calculated based on the weighted pixel value [23].

Here, we track the particles by utilizing the k-nearest neighbors algorithm. The algorithm classifies a query instance to the label that is most common amongst its k-nearest neighbors measured by a distance function. For our application, we chose k to be 1, this implies that a query particle p_s (in the current image) is simply classified to the label of its nearest neighbor (from the previous image). We defined an euclidean distance function for measuring the distances between the query particle p_s (in the current image) and all particles from the previous image. The euclidean distance function d_{eu} is expressed as

$$d_{eu}(s,f) = \sqrt{(l_s - l_f)^2 + (m_s - m_f)^2} \tag{12}$$

where parameters $l-$ and $m-$ are the two-dimensional coordinates of the particle in the image. The subscript s denotes the index of the query particle in the current image, and the subscript f refers to the label of the particle from the previous image.

C. CONTROL SCHEME

In this sub-section, we consider the problem of two-dimensional manipulation of multiple magnetic particles, and which the particles are subjected to random disturbances in their respective nominal positions.

This manipulation scenario could be applied to the case of manipulating the ECM stiffness for the investigation of cell-matrix mechanical interactions. In this case, the magnetic particles are to be firmly attached to the collagen fibers in the ECM and to be remained stationary in their respective (nominal) positions. However, if there is a perturbation in the ECM (which could be induced by the cell traction forces), the particles may be dislocated from their prescribed positions. By anchoring the particles (individually) in their nominal positions while they are subjected to possible cellular forces, the movements of the collagen fibres in the ECM are impeded. Hence, this possibly results in a change of apparent stiffness of the ECM as sensed by the cells.

Here, we devised a visual-servo control scheme to ensure the EMNC assembly (i.e. an end-effector) applies the necessary force on the dislocated particle to eliminate the dislocation.

1) DYNAMIC ANALYSIS OF THE PARTICLES

In this article, we focus on the motion of the particles in the $x-y$ plane (i.e. lateral plane). A magnetically controlled particle in the suspending medium (contained in a Petri-dish) mainly receives three forces: magnetic forces, disturbance forces, and viscous drag force. The dynamics equation of the particle is given by,

$$m\ddot{\mathbf{q}} = \mathbf{F_p} - \mathbf{F_{drag}} - \mathbf{F_{ds}} \tag{13}$$

where m is the mass of the particle, $\mathbf{q} \in \mathbb{R}^{2\times 1}$ is the position of the particle in the $x-y$ plane, $\mathbf{F_p} \in \mathbb{R}^{2\times 1}$ is the applied magnetic force, $\mathbf{F_{ds}} \in \mathbb{R}^{2\times 1}$ is the disturbance force, and $\mathbf{F_{drag}} \in \mathbb{R}^{2\times 1}$ is the viscous drag force. We neglected the interactions between the neighbouring particles, which is appropriate for dilute particle suspensions [24]. For the effect of the inertia force $m\ddot{\mathbf{q}}$, it is ignorable in the low Reynolds number environment [25]–[27]. As a result, (13) can be simplified as

$$0 = \mathbf{F_p} - \mathbf{F_{drag}} - \mathbf{F_{ds}} \tag{14}$$

According to the *Stokes'* law, the drag coefficient α of a spherical particle has the form of

$$\alpha = 6\pi\eta r_p \tag{15}$$

where r_p is the radius of the particle and η is the dynamic viscosity of the suspending medium. However, if the particle gets too close to the boundaries of the Petri-dish, it would incur a larger drag coefficient, which is then characterized by the *Faxen's* law [28] that states

$$\alpha = 6\pi\eta r_p\beta \tag{16}$$

where β is the correction factor (given by (17)) and h_p is the distance from the center of particle to the boundaries.

$$\beta = \left[1 - \frac{9}{16}\frac{r_p}{h_p} + \frac{1}{8}\frac{{r_p}^3}{{h_p}^3} - \frac{45}{256}\frac{{r_p}^4}{{h_p}^4} - \frac{1}{16}\left(\frac{{r_p}^5}{{h_p}^5}\right)^3\right]^{-1} \tag{17}$$

Hence, the drag force experienced by the particle is expressed as,

$$\mathbf{F_{drag}} = \alpha\dot{\mathbf{q}} \tag{18}$$

2) VISUAL-SERVO CONTROL SCHEME

A visual-servo control scheme is synthesized with the magnetic manipulation system to achieve (effectively) simultaneous manipulation of magnetic particles.

The control objective is to minimize the deviations of all particles in a selected ensemble from their desired positions, and which they are subjected to random perturbations. The position error $\mathbf{Er_g} \in \mathbb{R}^{2\times 1}$ of the particle g in the suspending medium is defined as

$$\mathbf{Er_g} = \mathbf{q_{d_g}} - \mathbf{q_g} \tag{19}$$

where $\mathbf{q_{d_g}} \in \mathbb{R}^{2\times 1}$ and $\mathbf{q_g} \in \mathbb{R}^{2\times 1}$ are the desired and the current positions of the particle g in the $x-y$ plane, with $g \in \{1, 2, \ldots, G\}$ and G equals to the total number of particles in the selected ensemble.

The control strategy is based on directing the localized magnetic force of the EMNC assembly to the respective desired positions of the particles. The system first identifies the locations of the particles and then maneuvers the EMNC to apply a localized magnetic force on the particles (one at a time but cyclically) to steer the particles and hold them in the vicinity of their respective desired positions. This level of control effectively achieves a simultaneous manipulation of multiple particles.

To realize this control scheme, the localized magnetic force intended for a particle must not affect other particles nearby, otherwise it would cause them to dislocate from their positions. Therefore, to minimize such proximity interference, the localized force area must be optimized. The localized area in this section is defined as a region within which $\mathbf{F_p} > (\mathbf{F_{drag}} + \mathbf{F_{ds}})$, such that (i) $\mathbf{F_p}$ induces a sufficient large force on the particle for effective manipulation and (ii) a localized area that is small enough without affecting the particles nearby. The particle within the localized area will be directed to the zero force point (as shown in Fig. 5(c)), and the localized area is ellipse-shaped (as shown in Fig. 5(b)).

The control strategy works by first determining (i) the particle g_l, which has the largest $Er_g = \|\mathbf{Er_g}\|_2$ (i.e. l_2- norm of $\mathbf{Er_g}$) in the ensemble, and (ii) the euclidean distances d_v of all the neighbouring particles to the particle g_l. The subscript v is the index for the neighbouring particles. Second, an algorithm is proposed to determine

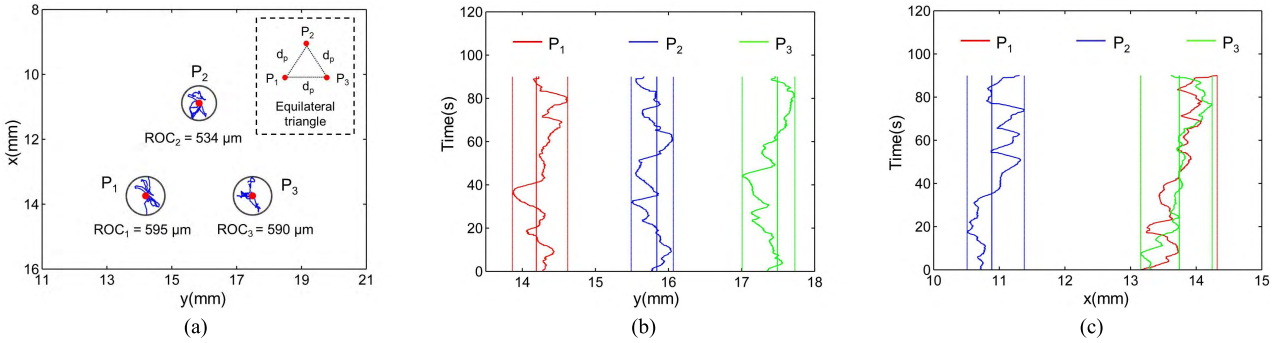

FIGURE 11. Representative closed-loop control of multiple magnetic particles. (a) Trajectories of the controlled particles towards their respective desired positions, and within a maximum region-of-convergence (ROC) of 595 μm in radius. ROCs are represented using black-dashed circles. (b) Motions of the particles towards their reference positions (solid vertical lines) along *y*-axis. (c) Motions of the particles towards their reference positions (solid vertical lines) along *x*-axis.

the input current of the EMN and the corresponding localized force area. This algorithm is realized by characterizing the magnetic force induced by the EMNC on the workspace, with the analytical model derived in Section II. Then, a lookup table (LUT) of the input currents I, to (i) the major radiuses r_{loc} of the localized force areas and (ii) the minimum forces $\mathbf{F_{p_{min}}}$, where $\mathbf{F_{p_{min}}} > (\mathbf{F_{drag}} + \mathbf{F_{ds}})$ is derived. The algorithm would first search for the nonzero minimum $\mathbf{F_{p_{min}}}$ in the LUT (to ensure the magnetic force is sufficient to manipulate the particle), and its corresponding input current I_{cl} and major radius of the localized area r_{cl}. Next, the r_{cl} is verified to be $< d_{v_{\min}}$ (where $d_{v_{\min}}$ is the euclidean distance of the closest neighbouring particle to particle g_l), and this is to warrant that the localized force area does not affect the particles nearby when manipulating particle g_l. Thereupon, the input current of the EMN will be specified as I_{cl}. Otherwise, if the closest neighbouring particle is too near to the particle g_l, such that $r_{cl} > d_{g_l\min}$, then the system will manipulate the subsequent particle with the next highest position error.

D. EXPERIMENT AND RESULTS

Experiments were carried out to demonstrate the effectiveness of the proposed system in simultaneous manipulation of multiple magnetic particles. Specifically, the experiments are to demonstrate the capability of the system in steering the magnetic particles to their respective desired positions and holding them in place, while they are constantly subjected to a random disturbance.

In these experiments, three paramagnetic particles (of 100 μm in diameter) were manipulated in deionized water with random perturbation. The particles and the suspending medium were contained in a standard Petri-dish (with a diameter of 150 mm). The magnetization curve of the paramagnetic particle is reported in Fig. 7. First, the system would position the three magnetic particles into an equilateral triangle formation as shown in the upper right inset of Fig. 11(a). The particles are marked by the red color circles and they are labeled as P_1, P_2, and P_3. These particles take their respective desired positions in the corners of the triangle, and the euclidean distances between the particles are of equal length d_p. Then, the random perturbation is introduced to dislocate the particles from their prescribed positions, and the proposed system would manipulate the particles (one at a time but cyclically) to eliminate the dislocations.

Fig. 11 shows the representative experimental results of the proposed system in manipulating the three paramagnetic particles. The motions of the three controlled particles are depicted in Fig. 11(a), the red color circles indicate the desired positions of the particles, and the blue lines are the trajectories of the particles during the experiment. Due to the disturbance forces, the proposed control system cannot achieve zero position tracking error as shown in Fig. 11(b) and 11(c). The system steers the particles (one at a time but cyclically) within the vicinity of their desired positions, which we refer to as a region-of-convergence as shown in Fig. 11(a). The radius of this region-of-convergence depends on the manipulation velocity of the particles, the disturbance forces, and the bandwidth of the control system (our vision system has a maximum frames-per-second of 90). In this representative experiment, the particles were controlled towards their reference positions (with $d_p = 3$ mm) at a manipulation velocity of 150 μm/*s*, and it resulted in a maximum region-of-convergence of 595 μm (in radius). This experiment is repeated five times, and the average maximum region-of-convergence are calculated to be 610$\pm$76 μm (in radius).

V. SUMMARY AND DISCUSSION

We have presented a magnetic manipulation system to achieve (effectively) simultaneous yet localized manipulation of multiple magnetic particles. The proposed system is equipped with a novel device that involves an EMN and a flux collector strategically positioned relative to each other to realize magnetic field and force localization. We first devised analytical models (using a system of magnetic dipoles) to determine the magnetic field and force in the vicinity of the designed EMNC. Next, experiments were carried out using a gauss meter with a hall sensor probe to validate the proposed magnetic field model. It was found that there were

discrepancies between the predicted and measured fields. There are two main factors that have contributed to the discrepancies; the first factor reflects the difference between the modeled and physical magnetic core. Our model considers the core as a stack of circular disk dipoles, whereas the physical core is a volume of point dipoles. The second factor involves the magnetization of the dipoles. Our model assumes each circular disk dipole is magnetized homogeneously, whereas the physical core of point dipoles magnetize inhomogeneously. Nevertheless, to achieve a quantitative agreement between both data, a multiplicative scaling function is introduced to both the EMN and the flux collector, respectively.

Based on proposed models, simulations were performed to investigate the localization effects of the EMNC assembly, and that of a single EMN in order to compare their effectiveness. The simulation results showed that the localization effects of the EMNC assembly on the magnetic field and force exhibited similar trends: (i) by reducing the distance between the tips of the EMN and the flux collector, and (ii) by increasing the angles of inclination (of the EMN and the flux collector), both the localized areas of magnetic field and force can be minimized up to 78.86% and 64.64%, respectively. The reason is that the flux collector effectively operates as a magnetic field sink, which provides a path for the emanated magnetic field from the EMN tip (i.e. magnetic field source). This reduces the distribution and concentrates the magnetic field between the EMN and collector tips. In view of the localization effects achieved with the EMNC assembly, the concept of the inclusion of the flux collector in localizing the magnetic field and force could possibly be extended to other forms of magnetic devices, where such localization effects are required.

With the characterized EMNC assembly, it is implemented to the magnetic manipulation system. Both hardware and software components of the manipulation system have been presented. The tracking of multiple magnetic particles using the center of mass algorithm and the *k*-nearest neighbors algorithm are presented, which is followed by the analysis of the dynamics of a magnetically controlled particle. Next, a visual-servo control scheme with an algorithm for determining the inputs (to control the localized force area of the EMNC assembly) is incorporated into the system to achieve (effectively) simultaneous manipulation of multiple magnetic particles. Experiments were conducted to demonstrate the effectiveness of the proposed system. The results show that the system are capable of controlling the magnetic particles within the vicinity of their reference positions (with an average maximum region-of-convergence of 610 ± 76 μm, in radius), while they were constantly subjected to a random perturbation.

However, there are a number of factors that limit the capability of the proposed system and device. First, the minimal area-of-influence of the magnetic force that can be achieved is inherently limited by the physical characteristics of the EMNC assembly. Owing to this fact, if the particles are too close to each other, especially in the extreme case, where particles are side by side to each other, the magnetic force generated by the EMNC may not be able to separate and manipulate them individually. A potential solution to resolve this issue is to design a more sophisticated control algorithm, such that the system is able to control the EMNC in attempt to exert an unbalanced force on the particles and separate them. Second, in this article, the focus is on the two-dimensional manipulation of multiple magnetic particles. To improve the applicability of the system for three-dimensional manipulation of particles, one possible solution is to have an additional inverted EMNC assembly place directly below of the samples. Third, the geometry of the flux collector tip needs to be investigated. It could have significant impacts in better localizing the magnetic field and force, which may lead to a more efficient EMNC device. Fourth, the effects of the localized magnetic force on a group of magnetic particles (instead of a single particle) remain to be explored. This would provide useful insights as to how particle-particle interacts within the localized area. It could be important for applications where particles could be drug-coated, since their interactions may initiate chemical or biochemical reactions. Last, the software of the proposed system should be developed with a programming language or environment that is more suited to cover a wider range of practical applications. One potential solution is to develop the software in MATLAB's Simulink (i.e. a graphical programming environment), and which it allows the incorporation of the developed algorithms/codes in MATLAB, by converting them into Simulink models. The recent advancements in MATLAB's Simulink have enabled users to build, run, and test real-time applications [29]–[31]. This is made possible with Simulink Real-Time, which automatically generates (based on the Simulink models) the program for embedded real-time applications. It can then be downloaded into a dedicated target computer/controller (equipped with real-time kernel, I/O interfaces, FPGAs, etc.) connected to the proposed physical system. Such an improvement in the software of the proposed system could reduce the computational time and so enhance the system's performance.

The above limiting factors notwithstanding, the work reported in this article in representing an initial effort to develop an engineering solution that enables simultaneous manipulation of multiple magnetic particles (i.e. the task to address individual particles and steer them independently). To the authors' best knowledge there is no existing method that achieves simultaneous yet localized manipulation of magnetic particles, specifically particles with the same geometrical and material properties. There are few reported works [32]–[34] that demonstrated individual manipulation of magnetic micro-structures in an ensemble. These untethered micro-structures were fabricated with size ranging from 70 μm to 1 mm for potential applications such as targeted drug-delivery and medical diagnosis. These works are usually accomplished through employing heterogeneous designs or materials. The working principle is that the

micro-structures would be excited via the same input signal (e.g. rotational or oscillating magnetic field), and with the different design parameters, these structures would exhibit different behaviors, such as variable actuation speeds or moving directions. For instance, in the work of [34], two mechanically unique micro-robots (which are coupled with different eigenfrequencies) were actuated by an oscillating magnetic field. The actuation of the robot occurs, when the frequency of the driving magnetic field is at the eigenfrequency of the robot's spring-mass system. These robots are then steered individually by alternating the input signal between their eigenfrequencies. The proposed system and the reported experimental results (in manipulating multiple magnetic particles) in this article complement the other published works, by extending the scope of magnetic manipulation from one single target to a group of them without the need for physically intricate micro-structures.

The proposed system has demonstrated its ability to manipulate magnetic particles individually and (effectively) simultaneously in an ensemble. The reported experimental results point to the possibilities in manipulating cells, biomolecules, micro-robots, and other micro-structures at multiple sites via direct application of localized and differentiated forces. However, there are two aspects to be noted in the implementation of the proposed system for practical applications. First, for a medium of a fixed volume, the number of particles and their proximity to each other for an effective manipulation depends on the viscosity of the medium, the size and magnetic properties of the particles, and the extent of the localization of the magnetic force. Second, the simultaneous manipulation of a group of particles is to be interpreted statistically, in the sense that all particle-position deviations will be corrected as fast as the visual-servo loop permits. Hence, it is possible that not all particles are manipulated to the same level of position accuracy. Consider the case where a random disturbance force severely dislocates a particular particle from its prescribed location in an ensemble. This will result in a longer time taken for the system to steer the particle back to its desired position. Therefore, this may incur larger position errors for the rest of the particles in the ensemble (since they are unattended for a longer period of time) and which then penalizes the accuracy of this manipulation approach.

One potential application of the proposed EMNC assembly in magnetic field localization is that it could be useful in transcranial magnetic stimulation (TMS) therapy for treating neuropsychiatric disorders. For the therapy, the key objective is to apply an electric field induced by a time-varying magnetic field on the human brain, which helps in stimulating under-active regions that are believed to be correlated to the disorders. However, the existing TMS devices suffer from a lack of magnetic field localization, leading to undesirable stimulation of other parts of the brain, and which can cause various adverse effects such as facial muscle activation and pain or discomfort [35]–[37]. Therefore, the EMNC assembly points to the prospect in being a viable TMS device for the therapy.

APPENDIX A
MAGNETIC SCALAR POTENTIAL OF A CE DIPOLE

Equation 4 is solved for a Ce_u dipole over a sub-interval $[z_{u_{i-1}}^{Ce'}, z_{u_i}^{Ce'}]$ and its scalar potential $\phi_{u_i}^{Ce}$ is expressed as

$$\begin{aligned}\phi_{u_i}^{Ce}(x,y,z) &= \frac{{r_{Cr_u}}^2 M_{u_{z_i}}^{Ce'}}{4{L_{Ce_u}}^2} \\ &\times \left(\frac{{z_{u_{i-1}}^{Ce'}}^2 - 4z_{u_{i-1}}^{Ce'} z + 2{c_1}^2 + 2zc_2 \ln(z_{u_{i-1}}^{Ce'} - z + c_2)}{c_2} \right. \\ &\left. - \frac{{z_{u_i}^{Ce'}}^2 - 4z_{u_i}^{Ce'} z + 2{c_1}^2 + 2zc_3 \ln(z_{u_i}^{Ce'} - z + c_3)}{c_3} \right) \\ c_1 &= \sqrt{(x^2+y^2+z^2)} \\ c_2 &= \sqrt{({z_{u_{i-1}}^{Ce'}}^2 - 2z_{u_{i-1}}^{Ce'} z + c_1^2)} \\ c_3 &= \sqrt{({z_{u_i}^{Ce'}}^2 - 2z_{u_i}^{Ce'} z + c_1^2)} \end{aligned} \tag{20}$$

where r_{Cr_u} is the radius of the magnetic core, and L_{Ce_u} is the length of the conical tip.

APPENDIX B
MAGNETIZATION OF A CE DIPOLE

The magnetic field strength $H_{sCyl_1}(z_{1_i}^{Ce'})$ is the summation of the field contributions by the electromagnetic coil and the magnetized Cyl_1, which can be expressed as

$$H_{sCyl_1}(z_{1_i}^{Ce'}) = H_s(z_{1_i}^{Ce'}) + H_{Cyl_1}(z_{1_i}^{Ce'}) \tag{21}$$

Consider a finite azimuthally symmetrical electromagnetic coil of length L_s and radius r_s with a number of turns per unit length n carrying a current I. Using the *Biot-Savart* law, the magnetic field contribution of an electromagnetic coil on the longitudinal axis is determined by modeling the coil as multiple current loops stacked together [38]. The magnetic field on the longitudinal axis is expressed as

$$\begin{aligned} H_s(z_1') &= \frac{nI}{2}\left(\frac{z_1' - d_w}{\sqrt{(z_1'-d_w)^2 + r_s^2}} - \frac{z_1' - e_w}{\sqrt{(z_1'-e_w)^2 + r_s^2}} \right) \\ d_w &= L_{Ce} \\ e_w &= L_{Ce} + L_s \end{aligned} \tag{22}$$

In consequence of the applied field from the coil, Cyl_1 is magnetized, and to determine its field contribution H_{Cyl_1}, the Cyl_1 is partitioned to M numbers of dipoles along the $z_1^{Cyl'}$-axis (i.e. z_1'-axis of Cyl_1). This is realized by dividing the interval $[L_{Ce_1}, L_{Cyl_1}]$ to sub-intervals of $\{[z_{1_N}^{Cyl'}, z_{1_{N+1}}^{Cyl'}], [z_{1_{N+1}}^{Cyl'}, z_{1_{N+2}}^{Cyl'}], \ldots, [z_{1_{M+N-1}}^{Cyl'} z_{1_{M+N}}^{Cyl'}]\}$, with each dipole spanning a sub-interval $[z_{1_{j-1}}^{Cyl'}, z_{1_j}^{Cyl'}]$. It has to be noted that both Cyl_1 and Ce_1 are in a common frame of reference and their origins are located at the tip. Equation 4 is solved for a Cyl_1 dipole over a sub-interval $[z_{1_{j-1}}^{Cyl'}, z_{1_j}^{Cyl'}]$ and

its scalar potential $\phi_{1_j}^{Cyl}$ is given by

$$\phi_{1_j}^{Cyl}(z_{1_i}^{Ce'}) = \frac{M_{1_{z_j}}^{Cyl'}}{2}\left(\sqrt{r_{Cr_1}^2 + (z_{1_i}^{Ce'} - z_{1_j}^{Cyl'})^2} - \sqrt{r_{Cr_1}^2 + (z_{1_i}^{Ce'} - z_{1_{j-1}}^{Cyl'})^2}\right) \quad (23)$$

where $M_{1_{z_j}}^{Cyl'}$ is the magnetization of the Cyl dipole, and which is dependent on $H_s(z_{1_j}^{Cyl'})$. The values of $M_{1_{z_j}}^{Cyl'}$ can be evaluated with $H_s(z_{1_j}^{Cyl'})$ from the magnetization curve of the core material. The total scalar potential of Cyl_1 (i.e. $\phi_{1_t}^{Cyl}$) at $z_{1_i}^{Ce'}$ is then approximated by the summation of the scalar potential of every Cyl_1 dipole over the length of Cyl_1, that is,

$$\phi_{1_t}^{Cyl}(z_{1_i}^{Ce'}) = \sum_{j=N+1}^{M+N} \phi_{1_j}^{Cyl}(z_{1_i}^{Ce'}) \quad (24)$$

By substituting (24) into (25), the magnetic field strength H_{Cyl1} at $z_{1_i}^{Ce'}$ can be evaluated.

$$H_{Cyl_1}(z_{1_i}^{Ce'}) = \frac{\partial \phi_{1_t}^{Cyl}}{\partial z_{1_i}^{Ce'}} \quad (25)$$

With the summation of $H_{Cyl_1}(z_{1_i}^{Ce'})$ and $H_s(z_{1_i}^{Ce'})$ in (21), the magnetic field strength $H_{sCyl_1}(z_{1_i}^{Ce'})$ can be determined. However, owing to the geometry of the conical-shaped tip, the magnetic flux is concentrated. For that reason, the field strength $H_{sCyl_1}(z_{1_i}^{Ce'})$ is amplified along the length of Ce_1, and the relationship is governed by

$$H_{sCyl_1}(z_{1_i}^{Ce'}) \propto \frac{1}{A_{Ce}(z_{1_i}^{Ce'})/A_{Ce}(z_{1_N}^{Ce'})} \quad (26)$$

where $A_{Ce}(z_{1_i}^{Ce'})$ is the cross sectional area of Ce_1 at $z_{1_i}^{Ce'}$.

REFERENCES

[1] K. E. Peyer, L. Zhang, and B. J. Nelson, "Bio-inspired magnetic swimming microrobots for biomedical applications," *Nanoscale*, vol. 5, no. 4, pp. 1259–1272, 2013.

[2] P. M. Oliver, J. S. Park, and D. Vezenov, "Quantitative high-resolution sensing of dna hybridization using magnetic tweezers with evanescent illumination," *Nanoscale*, vol. 3, no. 2, pp. 581–591, 2011.

[3] F. G. Schmidt, F. Ziemann, and E. Sackmann, "Shear field mapping in actin networks by using magnetic tweezers," *Eur. Biophys. J.*, vol. 24, no. 5, pp. 348–353, 1996.

[4] B. D. Matthews, D. R. Overby, R. Mannix, and D. E. Ingber, "Cellular adaptation to mechanical stress: Role of integrins, rho, cytoskeletal tension and mechanosensitive ion channels," *J. Cell Sci.*, vol. 119, no. 3, pp. 508–518, 2006.

[5] A. R. Bausch, F. Ziemann, A. A. Boulbitch, K. Jacobson, and E. Sackmann, "Local measurements of viscoelastic parameters of adherent cell surfaces by magnetic bead microrheometry," *Biophysical J.*, vol. 75, no. 4, pp. 2038–2049, 1998.

[6] Y. Tan, C.-W. Kong, S. Chen, S. H. Cheng, R. A. Li, and D. Sun, "Probing the mechanobiological properties of human embryonic stem cells in cardiac differentiation by optical tweezers," *J. Biomech.*, vol. 45, no. 1, pp. 123–128, 2012.

[7] E. U. Azeloglu and K. D. Costa, "Atomic force microscopy in mechanobiology: Measuring microelastic heterogeneity of living cells," in *Atomic Force Microscopy in Biomedical Research. Methods in Molecular Biology* (Methods and Protocols). New York, NY, USA: Humana Press, 2011, pp. 303–329.

[8] S. C. Herath *et al.*, "A magneto-microfluidic system for investigating the influence of an externally induced force gradient in a collagen type I ECM on HMVEC sprouting," *SLAS Technol., Transl. Life Sci. Innov.*, vol. 22, no. 4, pp. 413–424, 2017.

[9] H. H. See *et al.*, "An electromagnetic system for inducing a localized force gradient in an ECM and its influence on HMVEC sprouting," *SLAS Technol., Transl. Life Sci. Innov.*, vol. 23, no. 1, pp. 2017.

[10] S. C. Herath *et al.*, "Characterization of uniaxial stiffness of extracellular matrix embedded with magnetic beads via bio-conjugation and under the influence of an external magnetic field," *J. Mech. Behav. Biomed. Mater.*, vol. 30, pp. 253–265, Feb. 2014.

[11] S. C. Herath *et al.*, "Quantification of magnetically induced changes in ecm local apparent stiffness," *Biophys. J.*, vol. 106, no. 1, pp. 332–341, 2014.

[12] M. K. Yapici, A. E. Ozmetin, J. Zou, and D. G. Naugle, "Experimental characterization of micromachined electromagnetic probes using scanning hall probe microscopy," in *Proc. Solid-State Sens., Actuators Microsyst. Conf. Transducers*, 2007, pp. 2365–2368.

[13] M. K. Yapici, A. E. Ozmetin, J. Zou, and D. G. Naugle, "Development and experimental characterization of micromachined electromagnetic probes for biological manipulation and stimulation applications," *Sens. Actuators A, Phys.*, vol. 144, no. 1, pp. 213–221, 2008.

[14] N. Chomnawang, J.-B. Lee, and W. A. Davis, "Surface micromachined arch-shape on-chip 3-D solenoid inductors for high-frequency applications," *J. Micro/Nanolithograp., MEMS, MOEMS*, vol. 2, no. 4, pp. 275–281, 2003.

[15] H. Lu, B. Pillans, J.-C. Lee, and J.-B. Lee, "High aspect ratio air core solenoid inductors using an improved UV-LIGA process with contrast enhancement material," *Microsyst. Technol.*, vol. 13, nos. 3–4, pp. 237–243, 2007.

[16] J.-B. Yoon, B.-K. Kim, C.-H. Han, E. Yoon, K. Lee, and C.-K. Kim, "High-performance electroplated solenoid-type integrated inductor (SI^2) for RF applications using simple 3D surface micromachining technology," in *IEDM Tech. Dig.*, Dec. 1998, pp. 544–547.

[17] J. M. Coey, *Magnetism and Magnetic Materials*. Cambridge, U.K.: Cambridge Univ. Press, 2010.

[18] M. A. Heald and J. B. Marion, *Classical Electromagnetic Radiation*. North Chelmsford, MA, USA: Courier Corporation, 2012.

[19] L. Chen, A. Offenhäusser, and H.-J. Krause, "Magnetic tweezers with high permeability electromagnets for fast actuation of magnetic beads," *Rev. Sci. Instrum.*, vol. 86, no. 4, p. 044701, 2015.

[20] J. J. Abbott, O. Ergeneman, M. P. Kummer, A. M. Hirt, and B. J. Nelson, "Modeling magnetic torque and force for controlled manipulation of soft-magnetic bodies," *IEEE Trans. Robot.*, vol. 23, no. 6, pp. 1247–1252, Dec. 2007.

[21] M. P. Kummer, J. J. Abbott, B. E. Kratochvil, R. Borer, A. Sengul, and B. J. Nelson, "OctoMag: An electromagnetic system for 5-DOF wireless micromanipulation," *IEEE Trans. Robot.*, vol. 26, no. 6, pp. 1006–1017, Dec. 2010.

[22] D.-H. Kim, G. E. Georghiou, and C. Won, "Improved field localization in transcranial magnetic stimulation of the brain with the utilization of a conductive shield plate in the stimulator," *IEEE Trans. Biomed. Eng.*, vol. 53, no. 4, pp. 720–725, Apr. 2006.

[23] M. K. Cheezum, W. F. Walker, and W. H. Guilford, "Quantitative comparison of algorithms for tracking single fluorescent particles," *Biophys. J.*, vol. 81, no. 4, pp. 2378–2388, 2001.

[24] A. Sinha, R. Ganguly, A. K. De, and I. K. Puri, "Single magnetic particle dynamics in a microchannel," *Phys. Fluids*, vol. 19, no. 11, p. 117102, 2007.

[25] Z. Hu, J. Zhang, and J. Liang, "Experimental measurement and analysis of the optical trapping force acting on a yeast cell with a lensed optical fiber probe," *Opt. Laser Technol.*, vol. 39, no. 3, pp. 475–480, 2005.

[26] F. Arai, K. Yoshikawa, T. Sakami, and T. Fukuda, "Synchronized laser micromanipulation of multiple targets along each trajectory by single laser," *Appl. Phys. Lett.*, vol. 85, no. 19, pp. 4301–4303, 2004.

[27] Y. Wu, D. Sun, and W. Huang, "Mechanical force characterization in manipulating live cells with optical tweezers," *J. Biomech.*, vol. 44, no. 4, pp. 741–746, Feb. 2011.

[28] J. Happel and H. Brenner, *Low Reynolds Number Hydrodynamics*, vol. 2. The Hague, The Netherlands: Martinus Nijhoff, 1983, p. 27.
[29] A. K. Samanta, A. Naha, A. Routray, and A. K. Deb, "Fast and accurate spectral estimation for online detection of partial broken bar in induction motors," *Mech. Syst. Signal Process.*, vol. 98, pp. 63–77, Jan. 2018.
[30] I. Kardan, A. Akbarzadeh, and A. M. Mohammadi, "Real-time velocity scaling and obstacle avoidance for industrial robots using fuzzy dynamic movement primitives and virtual impedances," *Ind. Robot, Int. J.*, vol. 45, no. 1, pp. 110–126, 2018.
[31] F. Blaabjerg, B. Kędra, and R. Małkowski, "Energy storage device based on flywheel, power converters and simulink real-time," in *Proc. IEEE Int. Conf. Environ. Elect. Eng., IEEE Ind. Commercial Power Syst. Eur. (EEEIC/I&CPS Eur.)*, Jun. 2017, pp. 1–4.
[32] E. Diller, S. Floyd, C. Pawashe, and M. Sitti, "Control of multiple heterogeneous magnetic microrobots in two dimensions on nonspecialized surfaces," *IEEE Trans. Robot.*, vol. 28, no. 1, pp. 172–182, Feb. 2012.
[33] E. Diller, S. Miyashita, and M. Sitti, "Magnetic hysteresis for multi-state addressable magnetic microrobotic control," in *Proc. IEEE/RSJ Int. Conf. Intell. Robots Syst. (IROS)*, Oct. 2012, pp. 2325–2331.
[34] D. R. Frutiger, K. Vollmers, B. E. Kratochvil, and B. J. Nelson, "Small, fast, and under control: Wireless resonant magnetic micro-agents," *Int. J. Robot. Res.*, vol. 29, no. 5, pp. 613–636, 2010.
[35] P. G. Janicak *et al.*, "Transcranial magnetic stimulation in the treatment of major depressive disorder: A comprehensive summary of safety experience from acute exposure, extended exposure, and during reintroduction treatment," *J. Clin. Psychiatry*, vol. 69, no. 2, pp. 222–232, 2008.
[36] M. Hallet, "Transcranial magnetic stimulation and the human brain," *Nature*, vol. 406, no. 6792, pp. 147–150, Jul. 2000.
[37] E. H. Bae *et al.*, "Safety and tolerability of repetitive transcranial magnetic stimulation in patients with epilepsy: A review of the literature," *Epilepsy & Behav.*, vol. 10, no. 4, pp. 521–528, 2007.
[38] S. R. Muniz, V. S. Bagnato, and M. Bhattacharya, "Analysis of off-axis solenoid fields using the magnetic scalar potential: An application to a zeeman-slower for cold atoms," *Amer. J. Phys.*, vol. 83, no. 6, pp. 513–517, 2015.

HIAN HIAN SEE received the B.Eng. degree in mechanical engineering from the National University of Singapore in 2013, where she is currently pursuing the Ph.D. degree in mechanical engineering. Her main research interests include the development of magnetic manipulation techniques for bioengineering applications.

SAHAN C. B. HERATH received the bachelor's (Hons.) and Ph.D. degrees in mechanical engineering from the National University of Singapore in 2009 and 2014, respectively. From 2009 to 2014, he was a Research Scholar with the National University of Singapore. His research included the development of techniques for manipulating extracellular matrix stiffness through the application of precise magnetic fields on specialized microfluidic platforms for cellular growth and analysis.

YUE DU received the bachelor's degree from Northeast Agricultural University, the master's degree from the Harbin Institute of Technology, and the Ph.D. degree from the National University of Singapore. She has conducted a wide spectrum of research on engineered cellular characterization and manipulation and robot/biomanipulator design, with fruitful outcomes in both fundamental and applied research. She has involved in the projects funded by the Singapore-MIT Alliance for Research and Technology, Agency for Science, Technology and Research, and National Natural Science Foundation of China.

HARRY ASADA received the B.S., M.S., and Ph.D. degrees in precision engineering from Kyoto University, Kyoto, Japan, in 1973, 1975, and 1979, respectively.

He is currently a Ford Professor of mechanical engineering and the Director with the Brit and Alex d'Arbeloff Laboratory for Information Systems and Technology, Department of Mechanical Engineering, Massachusetts Institute of Technology (MIT), Cambridge, MA, USA. His robotics research interests include wearable robots, cellular PZT actuators, and robot applications to aircraft manufacturing and nuclear power plant monitoring. His research in the bio area focuses on biointegrated robots, where live cells and tissues are used as components. He specializes in robotics, biological engineering, and system dynamics and control.

Dr. Asada is a fellow of the American Society of Mechanical Engineers. He received Best Paper Awards from the IEEE International Conference on Robotics and Automation in 1993, 1997, 1999, and 2010, the O. Hugo Schuck Best Paper Award from the American Control Council in 1985, Best Journal Paper Awards from the Society of Instrument and Control Engineers in 1979, 1984, and 1990, and the Best Journal Paper Award from the Journal of Advanced Robotics in 2002. He also received the Henry Paynter Outstanding Researcher Award from ASME Dynamic Systems and Control in 1998. More recently, he received the 2011 Rufus Oldenburger Medal from ASME and the Ruth and Joel Spira Award for Distinguished Teaching from the School of Engineering, MIT.

PETER C. Y. CHEN received the Ph.D. degree from the University of Toronto, Canada, in 1995. From 1985 to 1997, he was involved in various projects for China International Marine Containers Ltd. (China), Automation Tooling Systems, Inc. (Canada), Electronics Division, General Dynamics Corp. (USA), Philips Pte. Ltd. (Singapore), the University of Toronto, CRS Robotics Inc. (Canada), and the Canadian Space Agency (Canada). From 1997 to 2000, he was a Research Fellow with the Singapore Institute of Manufacturing Technology. He joined the National University of Singapore in 2000, where he is currently an Associate Professor with the Department of Mechanical Engineering. His research interests include sensing, system dynamics, and control of biological system.